

Geomagnetic jerks and rapid hydromagnetic waves focusing at Earth's core surface

Julien Aubert^{1*} and Christopher C. Finlay²

Geomagnetic jerks are abrupt changes in the second time derivative—the secular acceleration—of Earth's magnetic field that punctuate ground observatory records. As their dynamical origin has not yet been established, they represent a major obstacle to the prediction of geomagnetic field behaviour for years to decades ahead. Recent jerks have been linked to short-lived, temporally alternating and equatorially localized pulses of secular acceleration observed in satellite data, associated with rapidly alternating flows at Earth's core surface. Here we show that these signatures can be reproduced in numerical simulations of the geodynamo that realistically account for the interaction between slow core convection and rapid hydromagnetic waves. In these simulations, jerks are caused by the arrival of localized Alfvén wave packets radiated from sudden buoyancy releases inside the core. As they reach the core surface, the waves focus their energy towards the equatorial plane and along lines of strong magnetic flux, creating sharp interannual changes in core flow and producing geomagnetic jerks through the induced variations in magnetic field acceleration. The ability to numerically reproduce jerks offers a new way to probe the physical properties of Earth's deep interior.

The geomagnetic field displays temporal variations on a broad range of timescales. Through a self-sustained dynamo process (the geodynamo), slow convective motion in Earth's electrically conducting and liquid core is believed to maintain the field and drive its changes over centuries and longer periods. At the other end of the range, geomagnetic jerks with typical timescales of a few years or less¹ represent the fastest observed features of the internally generated field. They were initially identified as 'V-shaped' patterns (see examples in Fig. 1a) in time series of the rate of change in the magnetic field at ground observatories^{2,3} (the secular variation), indicating an abrupt change in the field acceleration amid periods in which this acceleration is otherwise relatively constant. Explaining the timescale disparity between rapid jerks and slow convection is a theoretical challenge that has recently spurred substantial progress, both in observational geomagnetism and in numerical geodynamo simulations. In combination with an improving network of ground observatories, satellite magnetic field observations now provide a global and continuous view of geomagnetic secular acceleration over the past two decades^{4,5}, with a horizontal spatial resolution of approximately 2,000 km at the core surface (spherical harmonic degree 9) and a temporal resolution^{6,7} ranging from 1 yr on the largest scales (spherical harmonic degree 1) to approximately 3 yr (at spherical harmonic degree 9). This has markedly enhanced our empirical knowledge of jerks, most notably by revealing^{7–10} their links to short-lived, temporally and spatially alternating pulses of geomagnetic acceleration at the surface of the Earth (Fig. 1c,e), that at the core surface are often particularly prominent at low-to-mid-latitudes and localized in longitude (Fig. 2a,b, Supplementary Video 1). It has long been suspected that jerks could somehow represent the signature of hydromagnetic waves¹¹. This prompted an earlier explanation¹² for jerks in terms of time-varying zonal flows that are kinematically consistent with torsional Alfvén waves occurring between concentric, magnetically coupled axial cylinders in the core. Torsional waves have been successfully identified in Earth's core¹³, and in recent self-consistent numerical simulations of the

geodynamo^{14–18}, which have steadily improved over the past decade in rendering an increasingly realistic separation between the rapid Alfvén timescale (τ_A) controlling the hydromagnetic wave period and the slow timescale τ_U of convective overturn (U is the root-mean-squared velocity in the outer core; see Methods). However, the observations¹³ and numerical results¹⁷ point to $\tau_A \approx 2$ yr, shorter than earlier decadal estimates, and to torsional wave amplitudes that are too weak to account for the geomagnetic secular acceleration signal associated with jerks^{18,19}. Furthermore, the complex patterns of magnetic acceleration found in satellite observations require localized (that is, non-axisymmetric), rapidly alternating flows beneath the core surface^{5,20–22}. Taken together, these factors rule out a direct explanation of jerks in terms of torsional waves, but they do provide valuable new constraints on the rapid dynamics taking place in Earth's core.

Observed and simulated geomagnetic jerks

We analysed a suite of seven distinct numerical geodynamo simulations^{17,18} with variable control parameters that follow a well-defined path through parameter space that connects the region where the majority of existing models are found to the conditions of Earth's core (see Methods and Supplementary Table 1). A reasonably accurate large-scale approximation¹⁷ enables the exploration of parameters considerably beyond current computational limits for direct numerical simulations, and well within an asymptotic regime¹⁸ of rapid rotation and strong magnetic control (at and beyond 30% of the path) that pertains to the conditions in Earth's core. In our most advanced Midpath model (50% of the path), the value $\tau_A = 14.3$ yr implies hydromagnetic waves with interannual periods at wavelengths that are a fraction of the core size; this value is well separated from convective and magnetic diffusion processes with time scales of $\tau_U = 125$ yr and $\tau_\eta = 135,000$ yr, respectively. As τ_A is also much longer than the planetary rotation period ($\tau_\Omega = 0.19$ yr in the Midpath model), such periods are also well within the rotationally dominated range over which the Coriolis force plays a crucial role.

¹Université de Paris, Institut de Physique du Globe de Paris, CNRS, Paris, France. ²Division of Geomagnetism, National Space Institute, Technical University of Denmark, Lyngby, Denmark. *e-mail: aubert@ipgp.fr

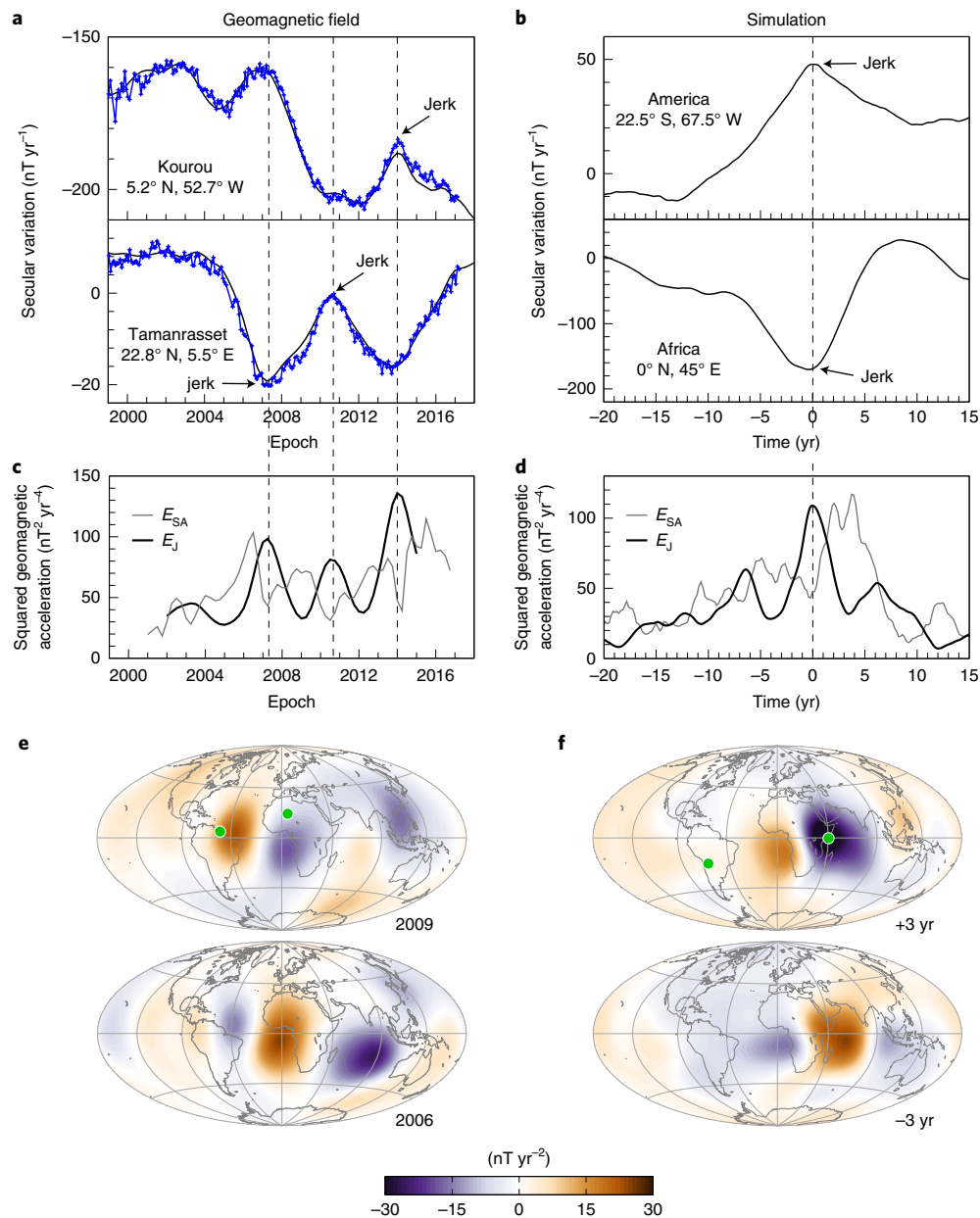


Fig. 1 | Observed and simulated geomagnetic jerks at Earth's surface. a,c,e. Observatory geomagnetic data from annual differences of revised monthly means (**a**, blue lines with crosses each month) and output from the CHAOS-6x5 geomagnetic field model⁵ (**a**, black lines, **c**, black and grey lines, and **e**) in the vicinity of recent geomagnetic jerks⁷⁻¹⁰ occurring near epochs 2007.5, 2011 and 2014 (dashed vertical lines). **b,d,f.** Output from the Midpath simulation in the vicinity of the main jerk event at 0 yr. **a,b.** Time series of the downward magnetic secular variation at real (**a**) and synthetic (**b**) observatories (located at the green dots in **e,f**). **c,d.** The secular acceleration and jerk energies E_{SA} (grey) and E_J (black, see Methods). **e,f.** Hammer projections of the radial secular acceleration (orange is outwards).

Our simulations spontaneously produce short-lived, intermittent pulses in the magnetic acceleration energy at Earth's surface (Fig. 1d). The spatial morphology and dynamical nature of the pulses become asymptotically robust from 30% of the parameter space onwards¹⁸, the region where our suite of models is located. The specific event from the Midpath model that we present in detail is representative of a majority¹⁸ of other events observed in the seven simulations, with the pulses reflecting intense low-to-mid-latitude magnetic acceleration activity at Earth's surface (Fig. 1f). To highlight the link between such pulses and jerks, and to facilitate comparison with geomagnetic field models with limited temporal resolution (Fig. 1c,e), we define the jerk energy (E_J , Methods) as the

mean squared difference between the time averages of Earth's surface magnetic acceleration taken within two consecutive and non-overlapping 3 yr time windows. Using this definition, the timing of jerks in the simulation (Fig. 1d) is found to either shortly precede or follow that of pulses of magnetic acceleration, as observed for well-documented recent geomagnetic jerks⁸ (Fig. 1c). The intensities and durations of the jerk events found in the simulations also match observations closely. Abrupt slope changes in the magnetic variation time series are observed at specific locations (Fig. 1b), with approximately constant acceleration away from the event, similar to the classic V-shaped jerk signatures seen at ground observatories¹⁻³ (Fig. 1a). Maps of the radial magnetic acceleration before and after

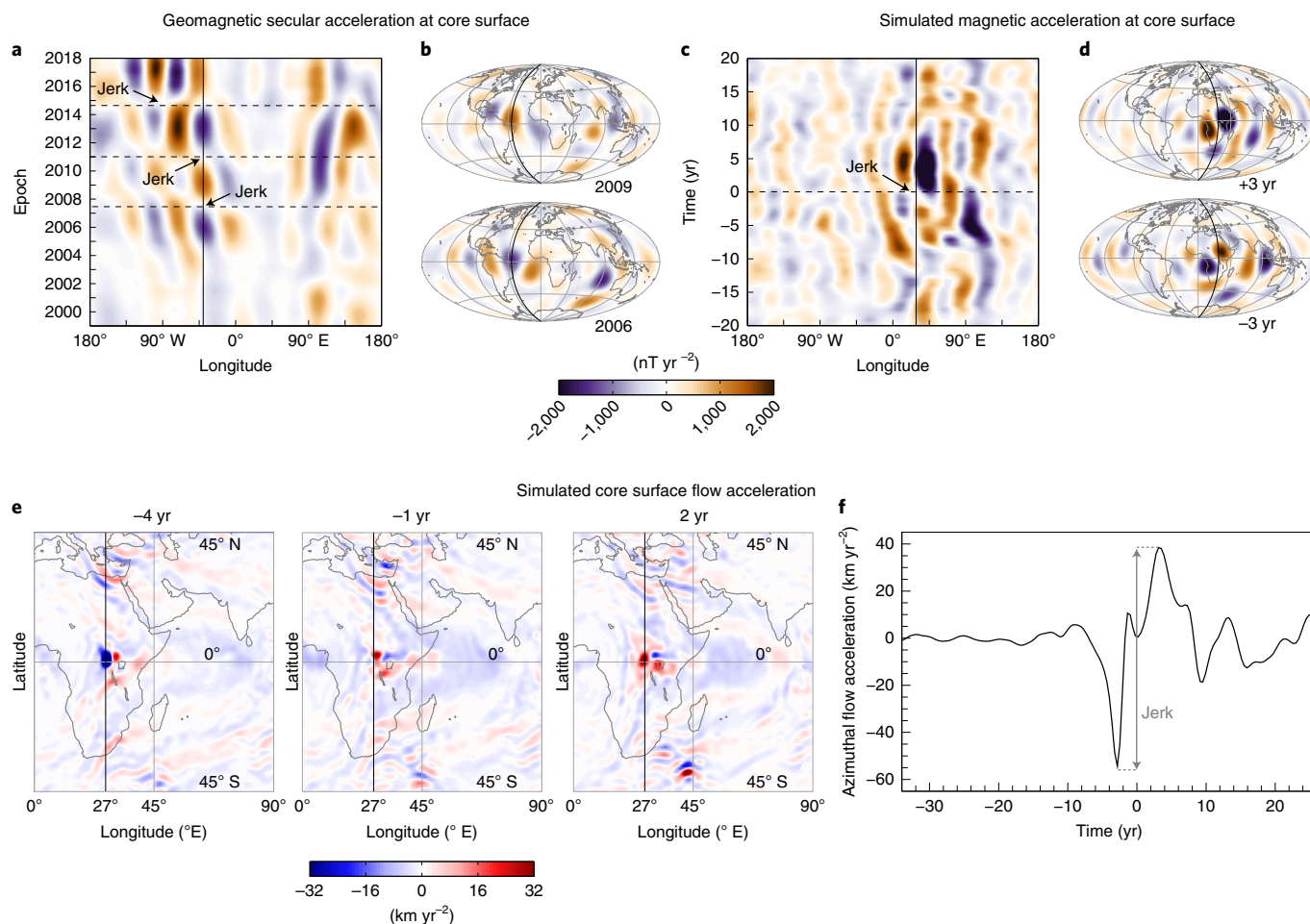


Fig. 2 | Comparison of the CHAOS-6x5 geomagnetic field model and the Midpath simulation at Earth's core surface. **a,c**, Time-longitude plots of equatorial radial magnetic secular acceleration (colour scale) filtered at spherical harmonic degree 9. Dashed horizontal lines locate jerk epochs. **b,d**, Hammer projections of the radial secular acceleration (same resolution as **a,c**) before (bottom) and after (top) jerk events (see Supplementary Videos 1 and 2). **e**, Miller projection of the core surface azimuthal flow acceleration (native model spatial resolution, blue is westwards, see colour scale) during the simulated jerk event (see Supplementary Video 3). Black vertical lines indicate specific longitudes selected for analysis in ref.⁵ for real events (**a-b**) and for the simulated event (**c-f**). **f**, Temporal evolution of the equatorial azimuthal flow acceleration at the analysis longitude.

the events feature alternating patterns (Fig. 1f) and indicate that simulated jerks are often visible over a large area (from the North and South American continents to Indonesia for the event shown here) at low and mid-latitudes, comparable to observations of the well-characterized 2007.5 geomagnetic jerk (Fig. 1e) and to a number of earlier events^{23,24}. Descending to the core surface (Fig. 2c,d), the most striking features are series of intense and oppositely signed patches of radial magnetic acceleration generated at low-to-mid-latitudes and in a narrow longitudinal band, beneath westward-drifting patches of intense radial magnetic flux^{18,25} (see Fig. 3e). The field acceleration patches alternate rapidly in time for a few years (Supplementary Video 2) before fading away. The spatially localized morphology, interannual alternation timescale and amplitude (approximately $2,000 \text{ nT yr}^{-2}$ up to spherical harmonic degree 9) of the simulation output reproduce well the core surface signature of recent geomagnetic jerks^{5,9} (Fig. 2a,b, Supplementary Video 1, see the events in 2007.5, 2011 and 2014.5).

Jerk mechanism and role of hydromagnetic waves

At the large scales accessible to observations at present (up to spherical harmonic degree 9), and in the rapid rotation regime, the magnetic acceleration pulses in the simulations result from the action of accelerating azimuthal core surface flows¹⁸ rather than from

diffusive processes related to flux expulsion that are common at the start of the parameter space path. In our Midpath model sequence, a localized, intense and temporally alternating pulse of azimuthal flow acceleration is observed in the vicinity of the jerk time (Fig. 2e,f, Supplementary Video 3), resembling the localized alternating flows that have been inferred from geomagnetic variations^{5,26} associated with recent geomagnetic jerks. The source of this perturbation in the simulation can be traced back to a sudden buoyancy release from the tip of an isolated density anomaly plume at mid-depth in the core 25 years before the event (Supplementary Videos 4 and 5). This release triggers strong azimuthal fluid flow accelerations that are entrained within the associated convective plume that ascends towards the core surface. The plume stalls at a cylindrical radius $s_c \approx 2,950 \text{ km}$ (Supplementary Video 4, Supplementary Fig. 1) where its decreasing radial velocity is overwhelmed by the global westward drift. At cylindrical radii above s_c , material upwelling stops or is even directed inwards, implying that only wave-driven propagation of energy outwards occurs beyond this point. Quasi-geostrophic Alfvén waves^{18,27} have previously been identified in this region; these share the same mechanism of magneto-inertial propagation along field lines as torsional waves, but differ in the sense that they develop at a non-axisymmetric level, provided that the background magnetic field created by the dynamo is sufficiently heterogeneous.

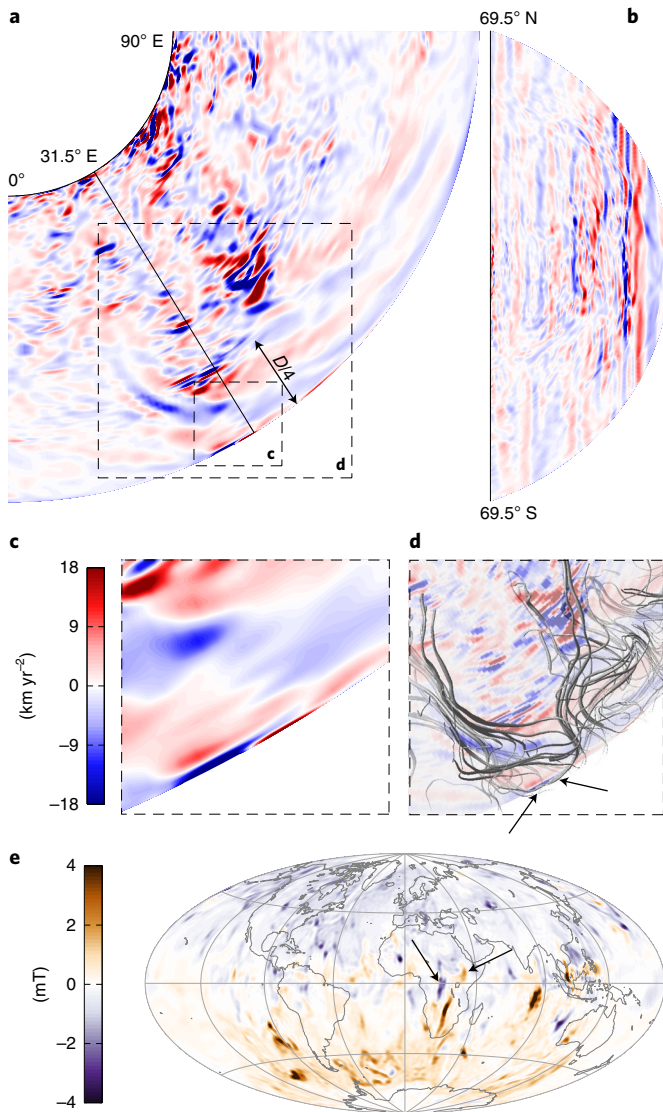


Fig. 3 | Hydromagnetic waves inside the core and magnetic field structure from the Midpath model. **a,b**, Azimuthal flow acceleration at -3.22 yr before the jerk event, in a partial equatorial planform (**a**) and a meridional planform (**b**) taken at the analysis longitude delineated in **a** and outside the axial cylinder tangent to the inner core (see Supplementary Video 5). **c**, Close-up view of the concentrated wave structures in **a** (see dashed box). **d**, Semi-transparent detail of **a** (see dashed box), with a volumetric rendering of the magnetic field lines overlaid (grey, thickness proportional to local field amplitude). **e**, Core surface radial magnetic field (native model spatial resolution, colour scale) at -3.22 yr in a Hammer projection. Arrows in **d,e** indicate the core surface magnetic flux patches where the focused waves emerge.

We have verified that the wave trajectories adhere to propagation at the locally variable, theoretical Alfvén wave speed and deviate from the paths of material upwellings (Methods and Supplementary Fig. 1). The perturbation energy propagates outwards towards the core surface in well-defined, azimuthally extended alternating wavefronts (Fig. 3a,b, Supplementary Video 5) of columnar structure that are characteristic of rotationally dominated dynamics¹⁸. The waves have a radial wavelength $d \approx D/4$ (where D is the thickness of the outer core) that is in line with the size of the density anomaly that initiated the event. Their energy becomes spatially concentrated as they approach the core–mantle boundary (Fig. 3c).

This yields the intense, localized and temporally alternating surface flow acceleration signature (Fig. 2e,f) that causes the jerk, on a fundamental timescale that is comparable to the Alfvén wave period for these structures, $\sqrt{3} \tau_A d/D \approx 6$ yr, with an undertone at 12 yr caused by the temporal modulation of the convective source. The energy concentration mechanism can be understood by noting that quasi-geostrophic Alfvén wavefronts are both guided along, and bounded by, a strongly heterogeneous distribution of magnetic field lines¹⁸. Beneath the jerk location, these field lines are arranged in an approximately axially invariant funnel-like structure (Fig. 3d) that is shaped by the slow convection and remains relatively static during the event. This causes the waves to be longitudinally focused towards a pair of intense radial magnetic flux patches (see arrows in Fig. 3e) at the core surface. At the same time, latitudinal focusing towards the Equator occurs because of the effect of the spherical core–mantle boundary on flow columns that tend to preserve their angular momentum as their height decreases (Fig. 3b, Supplementary Video 5). Finally, the wave speed decreases close to the core–mantle boundary (see curved green tracks in Supplementary Fig. 1) because the magnetic field is weaker at the surface than at depth¹⁷. To preserve the energy flux, the amplitude of wavefronts increases, and preservation of the wave period also implies a reduction of the radial wavelength (Fig. 3c), similar to a shoaling process for water waves²⁸. This three-dimensional energy-focusing mechanism is crucial to amplifying the weak quasi-geostrophic Alfvén waves to produce localized and temporally alternating disturbances in the core surface flow acceleration that are significant enough to cause jerks visible at Earth’s surface.

Other important details of observed geomagnetic jerks can be accounted for by the properties of quasi-geostrophic Alfvén waves triggered in this fashion. First, the columnar wave patterns emitted from the buoyancy release can also cause significant alternating flow and magnetic field acceleration at mid-to-high latitudes (Fig. 2d,e, Supplementary Videos 2 and 3 from -4 yr to 0 yr, in the Southern Hemisphere). Off-Equator focusing can then occasionally lead to events with foci at such latitudes¹⁸, similar to the 1969 and 1978 geomagnetic jerks^{1,29–32}. Second, the perturbation is communicated to other longitudes by the elongated eastern flank of the wave (Fig. 3a). As the background magnetic field pattern (Fig. 3e) allows for multiple focusing points at the core–mantle boundary, this can lead to several quasi-synchronized wave arrivals at longitudinally remote locations, with corresponding magnetic acceleration signals that broaden the extent of the jerk (Fig. 2d, Supplementary Videos 2 and 3, time -4 yr, see equatorial flow and magnetic acceleration west of America). This effect is similar to the long-range interconnection of alternating magnetic acceleration flux patches observed during well-documented geomagnetic jerks^{9,21,32,33}, as seen in Fig. 2a,b and Supplementary Video 1, for instance, where acceleration structures below America and Asia tend to evolve in a synchronized manner. Third, due to the background magnetic field and flow geometry in which it evolves, the elongated wavefront does not arrive simultaneously at the core–mantle boundary, with arrival time dependent on the longitude. This geometry results in a rapid apparent westward propagation of the alternating secular acceleration patches (Fig. 2c) that adds to the slower background westward drift.

Implications for geomagnetism and global geodynamics

As our models are in the dynamical regime of rapid rotation and strong magnetic control relevant to Earth’s core^{17,18}, their results can be extrapolated to natural conditions. According to the mechanism described here, the duration and alternation timescale of jerk events are expected to scale with τ_A , which is about seven times shorter in Earth’s core¹³ than in our Midpath simulation (Supplementary Table 1). Yet the observed geomagnetic acceleration changes are only two to three times faster than those simulated by the Midpath model

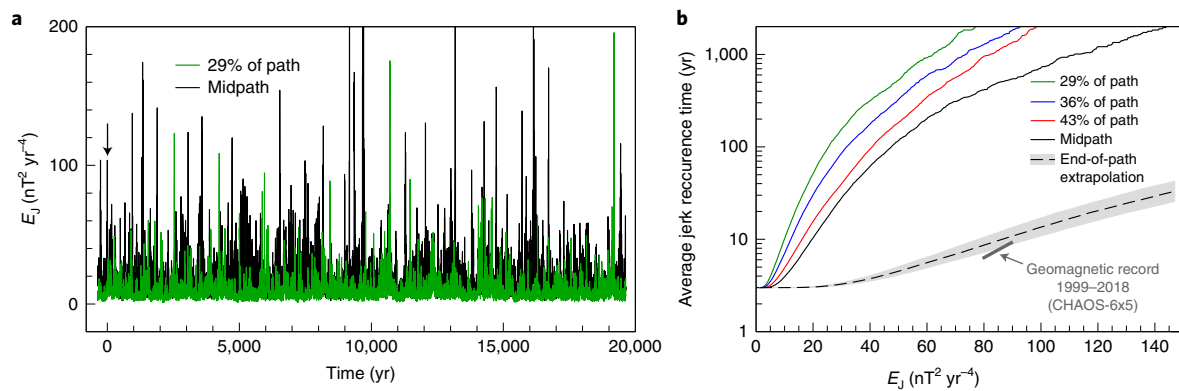


Fig. 4 | Statistics of jerk recurrence time. **a**, Time series of E_j (see Methods) in the 29% of path and Midpath models (Supplementary Table 1). The arrow indicates the event analysed in Figs. 1–3. **b**, Distribution of the average recurrence time of jerks reaching or exceeding a given energy for models within the rapid rotation regime¹⁸ (solid lines). An extrapolation (see Methods and Supplementary Fig. 2) of the recurrence time distribution for the Earth's core conditions is also shown (the shaded envelope represents the ± 1 s.d. uncertainty area). The dark grey line segment indicates the output of CHAOS-6x5 as estimated from Fig. 1c (three jerks with $E_j \geq 80 \text{ nT}^2 \text{ yr}^{-4}$ and two with $E_j \geq 90 \text{ nT}^2 \text{ yr}^{-4}$ within 19 yr).

(Fig. 2). This discrepancy is probably related to the limited temporal resolution of geomagnetic field models, which prevents the true, potentially sub-annual^{33,34} variations associated with jerks from being retrieved at present. If such is the case, the observed signals are representative of the longest undertones of the Alfvén wave packet. In upcoming years, insight into this issue will be obtained from further jerk events that will be imaged with improved resolution using data collected by the Swarm satellite mission and improved models for external contributions. Another difference involves the sequence of secular acceleration pulses of alternating sign that has been observed in relation with recent jerks (Figs. 1c and 2a). Such features can be explained in our models by the arrival of successive quasi-geostrophic Alfvén wavefronts (Figs. 1d and 2c). However, in the simulation presented in detail here, we only see two significantly weaker jerks (at -6 yr and $+6$ yr, Fig. 1d) on each side of the main jerk. This difference is a consequence of the wave damping factor, which although weak in the Midpath model (as evidenced by the ratio $\tau_A/\tau_\eta \approx 10^{-4}$) is still seven times stronger than expected in Earth's core. As we move along the parameter space path, our models indicate that energetic jerks occur more frequently (Fig. 4a). It is possible to construct statistical relationships between jerk energy and recurrence time (Fig. 4b), and derive a scaling relationship for the evolution along the path of jerk energy at a given recurrence time (Supplementary Fig. 2) that is in reasonable agreement with a theoretical prediction (see Methods). The extrapolation of this relationship to the end of the path (Fig. 4b) is also in agreement with the observed sub-decadal to decadal jerk recurrence rates observed in the geomagnetic field^{1,5}. Jerk energy is also found to decrease with increasing lower mantle conductance, because of the associated additional Ohmic losses, and with increasing levels of stratification in the upper outer core (Supplementary Fig. 3). This latter effect is due to changes in the geometry and amplitude of the background magnetic field^{35,36} rather than to the wave mechanism itself, which is not sensitive to stratification. Finally, examining simulated records of the length of day (Methods, Supplementary Fig. 4) in the vicinity of jerk events, we also observe signatures of the quasi-geostrophic Alfvén wave's arrival at the core surface. Rapid inflexions in the rate of change of the length-of-day similar to those observed for Earth^{24,37} are caused by pulses in the acceleration of the electromagnetic torque felt by the mantle. These results highlight the potential importance of the numerical reproduction of jerks, as it may lead to an improved geomagnetic^{38,39} and geodetic⁴⁰ sounding of crucial, but poorly known physical properties such as the lower mantle electrical conductivity and upper outer core thermal conductivity.

The integration of geomagnetic data into numerical geodynamo simulations through data assimilation has considerably advanced in recent years⁴¹, leading to preliminary inferences of the dynamical internal structure of the geodynamo and to predictions of the future evolution of the geomagnetic field⁴² that have been integrated within the latest iteration^{43,44} of the International Geomagnetic Reference Field. At interannual to decadal timescales, the accuracy of such predictions is currently hampered by the underlying dynamical model, which is located at the start of the parameter space path and hence does not correctly account for hydromagnetic wave dynamics. The availability of advanced numerical dynamo simulations that produce realistic rapid dynamics and jerks will substantially improve the quality of the prior information on which the predictions are based (particularly the time-dependence of the field), with subsequent gains in the accuracy of these predictions.

Online content

Any methods, additional references, Nature Research reporting summaries, source data, extended data, supplementary information, acknowledgements, peer review information; details of author contributions and competing interests; and statements of data availability and code availability are available at <https://doi.org/10.1038/s41561-019-0355-1>.

Received: 19 April 2018; Accepted: 15 March 2019;

Published online: 22 April 2019

References

- Brown, W., Mound, J. & Livermore, P. Jerks abound: an analysis of geomagnetic observatory data from 1957 to 2008. *Phys. Earth Planet. Int.* **223**, 62–76 (2013).
- Courillot, V., Ducruix, J. & Le Mouél, J.-L. Sur une accélération récente de la variation séculaire du champ magnétique terrestre. *C. R. Acad. Sci. Paris D* **287**, 1095–1098 (1978).
- Malin, S. R. C., Hodder, B. M. & Barraclough, D. R. in *Scientific Contributions in Commemoration of Ebro Observatory's 75th Anniversary* (ed. Cardús, J. O.) 239–256 (Observatorio Del Ebro, 1983).
- Lesur, V., Wardinski, I., Hamoudi, M. & Rother, M. The second generation of the GFZ reference internal magnetic model: GRIMM-2. *Earth Planets Space* **62**, 765–773 (2010).
- Finlay, C. C., Olsen, N., Kotsiaros, S., Gillet, N. & Toffner-Clausen, L. Recent geomagnetic secular variation from Swarm and ground observatories as estimated in the CHAOS-6 geomagnetic field model. *Earth Planets Space* **68**, 112 (2016).

6. Olsen, N., Manda, M., Sabaka, T. J. & Toffner-Clausen, L. CHAOS-2—a geomagnetic field model derived from one decade of continuous satellite data. *Geophys. J. Int.* **179**, 1477–1487 (2009).
7. Chulliat, A. & Maus, S. Geomagnetic secular acceleration, jerks, and a localized standing wave at the core surface from 2000 to 2010. *J. Geophys. Res.* **119**, 1531–1543 (2014).
8. Chulliat, A., Thebaud, E. & Hulot, G. Core field acceleration pulse as a common cause of the 2003 and 2007 geomagnetic jerks. *Geophys. Res. Lett.* **37**, L07301 (2010).
9. Chulliat, A., Alken, P. & Maus, S. Fast equatorial waves propagating at the top of the Earth's core. *Geophys. Res. Lett.* **42**, 3321–3329 (2015).
10. Torta, J. M., Pavón-Carrasco, F. J., Marsal, S. & Finlay, C. C. Evidence for a new geomagnetic jerk in 2014. *Geophys. Res. Lett.* **42**, 7933–7940 (2015).
11. Braginsky, S. I. Short-period geomagnetic secular variation. *Geophys. Astrophys. Fluid Dynam.* **30**, 1–78 (1984).
12. Bloxham, J., Zatman, S. & Dumberry, M. The origin of geomagnetic jerks. *Nature* **420**, 65–68 (2002).
13. Gillet, N., Jault, D., Canet, E. & Fournier, A. Fast torsional waves and strong magnetic field within the Earth's core. *Nature* **465**, 74–77 (2010).
14. Wicht, J. & Christensen, U. R. Torsional oscillations in dynamo simulations. *Geophys. J. Int.* **181**, 1367–1380 (2010).
15. Teed, R. J., Jones, C. A. & Tobias, S. M. The dynamics and excitation of torsional waves in geodynamo simulations. *Geophys. J. Int.* **196**, 724–735 (2014).
16. Schaeffer, N., Jault, D., Nataf, H.-C. & Fournier, A. Turbulent geodynamo simulations: a leap towards Earth's core. *Geophys. J. Int.* **211**, 1–29 (2017).
17. Aubert, J., Gastine, T. & Fournier, A. Spherical convective dynamos in the rapidly rotating asymptotic regime. *J. Fluid Mech.* **813**, 558–593 (2017).
18. Aubert, J. Geomagnetic acceleration and rapid hydromagnetic wave dynamics in advanced numerical simulations of the geodynamo. *Geophys. J. Int.* **214**, 531–547 (2018).
19. Cox, G., Livermore, P. & Mound, J. The observational signature of modelled torsional waves and comparison to geomagnetic jerks. *Phys. Earth Planet. Int.* **255**, 50–65 (2016).
20. Wardinski, I., Holme, R., Asari, S. & Manda, M. The 2003 geomagnetic jerk and its relation to the core surface flows. *Earth Planet. Sci. Lett.* **267**, 468–481 (2008).
21. Silva, L. & Hulot, G. Investigating the 2003 geomagnetic jerk by simultaneous inversion of the secular variation and acceleration for both the core flow and its acceleration. *Phys. Earth Planet. Int.* **198–199**, 28–50 (2012).
22. Gillet, N., Jault, D. & Finlay, C. C. Planetary gyre, time-dependent eddies, torsional waves and equatorial jets at the Earth's core surface. *J. Geophys. Res.* **120**, 3991–4013 (2015).
23. Dormy, E. & Manda, M. Tracking geomagnetic impulses at the core–mantle boundary. *Earth Planet. Sci. Lett.* **237**, 300–309 (2005).
24. Manda, M. et al. Geomagnetic jerks: rapid core field variations and core dynamics. *Space Sci. Rev.* **155**, 147–175 (2010).
25. Aubert, J., Finlay, C. C. & Fournier, A. Bottom-up control of geomagnetic secular variation by the Earth's inner core. *Nature* **502**, 219–223 (2013).
26. Kloss, C. & Finlay, C. C. Time-dependent low-latitude core flow and geomagnetic field acceleration pulses. *Geophys. J. Int.* **217**, 140–168 (2019).
27. Bardsley, O. P. & Davidson, P. A. Inertial–Alfvén waves as columnar helices in planetary cores. *J. Fluid Mech.* **805**, R2 (2016).
28. Dean, R. G. & Dalrymple, R. A. *Water Wave Mechanics for Engineers and Scientists* Vol. 2 (World Scientific, 1991).
29. Le Huy, M., Alexandrescu, M., Hulot, G. & Le Mouél, J.-L. On the characteristics of successive geomagnetic jerks. *Earth Planets Space* **50**, 723–732 (1998).
30. Sabaka, T. J., Olsen, N. & Purucker, M. Extending comprehensive models of the Earth's magnetic field with Oersted and CHAMP data. *Geophys. J. Int.* **159**, 521–547 (2004).
31. Pinheiro, K. J., Jackson, A. & Finlay, C. C. Measurements and uncertainties of the occurrence time of the 1969, 1978, 1991, and 1999 geomagnetic jerks. *Geochem. Geophys. Geosyst.* **12**, Q10015 (2011).
32. Pais, M. A., Alberto, P. & Pinheiro, F. J. G. Time-correlated patterns from spherical harmonic expansions: Application to geomagnetism. *J. Geophys. Res.* **120**, 8012–8030 (2015).
33. Olsen, N. & Manda, M. Rapidly changing flows in the Earth's core. *Nat. Geosci.* **1**, 390–394 (2008).
34. Gillet, N. in *Geomagnetism, Aeronomy and Space Weather: A Journey from the Earth's Core to the Sun* (eds Manda, M. et al.) Ch. 9 (International Association of Geomagnetism and Aeronomy, 2019).
35. Nakagawa, T. Effect of a stably stratified layer near the outer boundary in numerical simulations of a magnetohydrodynamic dynamo in a rotating spherical shell and its implications for Earth's core. *Phys. Earth Planet. Int.* **187**, 342–352 (2011).
36. Christensen, U. R. Geodynamo models with a stable layer and heterogeneous heat flow at the top of the core. *Geophys. J. Int.* **215**, 1338–1351 (2018).
37. Holme, R. & de Viron, O. Geomagnetic jerks and a high-resolution length-of-day profile for core studies. *Geophys. J. Int.* **160**, 435–439 (2005).
38. Lesur, V., Whaler, K. & Wardinski, I. Are geomagnetic data consistent with stably stratified flow at the core–mantle boundary? *Geophys. J. Int.* **201**, 929–946 (2015).
39. Schaeffer, N. & Jault, D. Electrical conductivity of the lowermost mantle explains absorption of core torsional waves at the equator. *Geophys. Res. Lett.* **43**, 4922–4928 (2016).
40. Holme, R. & de Viron, O. Characterization and implications of intradecadal variations in length of day. *Nature* **499**, 202–204 (2013).
41. Fournier, A. et al. An Introduction to data assimilation and predictability in geomagnetism. *Space Sci. Rev.* **155**, 247–291 (2010).
42. Aubert, J. Geomagnetic forecasts driven by thermal wind dynamics in the Earth's core. *Geophys. J. Int.* **203**, 1738–1751 (2015).
43. Fournier, A., Aubert, J. & Thébaud, E. A candidate secular variation model for IGRF-12 based on Swarm data and inverse geodynamo modelling. *Earth Planets Space* **67**, 81 (2015).
44. Thébaud, E. et al. International geomagnetic reference field: the twelfth generation. *Earth Planets Space* **67**, 79 (2015).

Acknowledgements

J.A. acknowledges support from the French Programme National de Planétologie of CNRS/INSU, and from the Fondation Simone et Cino Del Duca of Institut de France (2017 research grant). This work was granted access to the HPC resources of S-CAPAD, IPGP, France, and to the HPC resources of IDRIS, CINES and TGCC under allocations A0020402122 and A0040402122 from GENCI. The results presented in this work rely on data collected at magnetic observatories. The authors thank the national institutes that support them and INTERMAGNET for promoting high standards of magnetic observatory practice (www.intermagnet.org). This is IPGP contribution 4011.

Author contributions

J.A. designed the project, designed and carried out the numerical experiments and wrote the manuscript. C.C.F. processed the geomagnetic data, constructed the CHAOS-6x5 geomagnetic field model and led its comparison with the simulation results. J.A. and C.C.F. processed the results and discussed the manuscript.

Competing interests

The authors declare no competing interests.

Additional information

Supplementary information is available for this paper at <https://doi.org/10.1038/s41561-019-0355-1>.

Reprints and permissions information is available at www.nature.com/reprints.

Correspondence and requests for materials should be addressed to J.A.

Publisher's note: Springer Nature remains neutral with regard to jurisdictional claims in published maps and institutional affiliations.

© The Author(s), under exclusive licence to Springer Nature Limited 2019

Methods

Model description. The full description of our numerical models can be found in refs.^{17,18}. The outer core is modelled as a rotating spherical shell of thickness $D = r_o - r_i$ (where r_i and r_o are the inner and outer core radii, respectively) filled with an electrically conducting fluid, with $r_i/r_o = 0.35$ as in Earth. In this domain, we solve the equations of Boussinesq convection, thermochemical density anomaly transport and magnetic induction in the magnetohydrodynamic approximation. Our unknowns are the velocity field \mathbf{u} , magnetic field \mathbf{B} and density anomaly field C , and we analyse the magnetic variation $\partial\mathbf{B}/\partial t$, magnetic acceleration $\partial^2\mathbf{B}/\partial t^2$ and the flow acceleration $\partial\mathbf{u}/\partial t$ at time t . The inner core and mantle are respectively modelled as a solid sphere of radius r_i and a solid shell between radii r_o and $1.83r_o$, both of which are electrically conducting and therefore electromagnetically coupled to the outer core. The inner core and mantle are also coupled by a gravitational restoring torque, and the net torque felt by each layer determines the time dependency of its axial differential rotation with respect to the outer core. Moments of inertia for the inner core, outer core and mantle respect the proportions²⁵ relevant to Earth, and the constant angular momentum of the ensemble defines the planetary rotation rate Ω .

The mechanical boundary conditions used for the outer core are of the stress-free type. In the low-viscosity regime where our models operate, these are undistinguishable from no-slip conditions¹⁷ and remove the need to resolve viscous boundary layers that would have thicknesses of <1km, much thinner than any dynamical structure of interest here. Electrically conducting boundary conditions are also used for the outer core. The entire inner core has the same electrical conductivity σ_c as the outer core. The mantle is conducting only in a basal region of thickness Δ and conductivity σ_m . In our four main model cases (Supplementary Table 1), the dimensionless conductance is set to a median geophysical estimate⁴⁵ $\Sigma = \Delta\sigma_m/D\sigma_c = 10^{-4}$. Two other models (Midpath-I and Midpath-H) explore the end-member values $\Sigma = 0$ (insulating mantle) and $\Sigma = 10^{-3}$.

The thermochemical conditions at the boundaries of the outer core are of the heterogeneous, fixed-flux type. The homogeneous part F of the density anomaly flux is prescribed at the inner boundary. In our four main model cases the homogeneous density anomaly flux vanishes at the outer boundary (neutral buoyancy). A sink term is introduced in the equation for thermochemical density anomaly transport in order to conserve mass. Within the Boussinesq approximation, this configuration models thermochemical convection driven by inner core freezing that reaches up to the core–mantle boundary, where heat flow is exactly adiabatic. An extra model (Midpath-S) explores the effect of a possible stratification of the upper outer core⁴⁶ by prescribing a negative (adverse buoyancy) density anomaly flux at the core–mantle boundary (see the Stratified core section below). Spatial modulations of the density anomaly fluxes are prescribed at both boundaries¹⁸, with the same geometry as in our previous coupled Earth model²⁵. These are meant to model heterogeneities in the growth of the inner core and thermal mantle control.

Model parameters, parameter space path and timescales. The model is controlled by four main dimensionless parameters, the flux-based Rayleigh, Ekman, Prandtl and magnetic Prandtl numbers

$$Ra_F = \frac{g_o F}{4\pi\rho\Omega^3 D^4} \tag{1}$$

$$E = \frac{\nu}{\Omega D^2} \tag{2}$$

$$Pr = \frac{\nu}{\kappa} \tag{3}$$

$$Pm = \frac{\nu}{\eta} \tag{4}$$

Here g_o , ρ , ν , κ and η are the gravity at the core–mantle boundary, fluid density, viscosity and thermochemical and magnetic diffusivities ($\eta = 1/\mu\sigma_c$, where μ is the fluid magnetic permeability). In our suite of models, the control parameters follow a unidimensional path¹⁷ in parameter space that connects the conditions of our previous coupled Earth (CE) model²⁵ to those of the Earth’s core. A single variable ϵ controls the four parameters through the following rules:

$$Ra_F = \epsilon Ra_F(CE) \tag{5}$$

$$E = \epsilon E(CE) \tag{6}$$

$$Pr = 1 \tag{7}$$

$$Pm = \sqrt{\epsilon} Pm(CE) \tag{8}$$

Here $Ra_F(CE) = 2.7 \cdot 10^{-5}$, $E(CE) = 3 \cdot 10^{-5}$ and $Pm(CE) = 2.5$ are the control parameters of the CE model at the start of the path ($\epsilon = 1$). We have shown¹⁷ that parameters that realistically describe Earth’s core conditions can be obtained by setting $\epsilon = 10^{-7}$, which defines the end of the path. Our main model cases are defined in refs.^{17,18} and in Supplementary Table 1 by the values $\epsilon = 10^{-2}$, $3.33 \cdot 10^{-3}$, 10^{-3} and $3.33 \cdot 10^{-4}$, respectively corresponding to 29%, 36%, 43% and 50% of the path (the Midpath model).

The model outputs follow scaling laws¹⁷ depending on ϵ that also closely approach the conditions expected in Earth’s core as we progress along the path (Supplementary Table 1). Once the magnetic diffusion time $\tau_\eta = D^2/\eta$ is set to an Earth-like value (see Rescaling section), the end of path simultaneously matches the Earth’s core rotational time $\tau_\Omega = 2\pi/\Omega$, convective overturn time $\tau_U = D/U$, and Alfvén time $\tau_A = \sqrt{\rho\mu}D/B$ (here B is the dynamo-generated magnetic field in the fluid shell). This confirms the continuous physical progression of our suite of models towards Earth’s core conditions. The dimensional values of τ_Ω , τ_U and τ_A reached in our models and at the end of path are listed together with Earth’s core estimates in Supplementary Table 1 (see ref.¹⁸ for a complete list of dimensionless timescale ratios achieved in the models).

Dimensional rescaling of dimensionless model output. The dimensionless model length unit is adjusted to the thickness $D = 2,260$ km of Earth’s core. Time is rescaled by adjusting the magnetic diffusion timescale $\tau_\eta = D^2/\eta$ to the value $\tau_\eta = 135,000$ yr, corresponding to a value $\eta = 1.2 \text{ m}^2 \text{ s}^{-1}$ at the midpoint of current estimates¹⁷. Given the invariance of $Rm = \tau_\eta/\tau_U \approx 1,000$ along the parameter space path, this rescaling choice ensures $\tau_U \approx 130$ yr and Earth-like convective geomagnetic variations¹⁸. The fluid and Alfvén wave velocities are rescaled by using these length and time units. The magnetic field amplitude is presented by setting the Elsasser magnetic field unit $\sqrt{\rho\mu\eta\Omega}$ to the value 0.9 mT. Given the approximate invariance of the Elsasser number $B^2/\rho\mu\eta\Omega \approx 20$ along the path¹⁷, this corresponds to setting the root-mean-squared field amplitude within the core to a value of about 4 mT, in agreement with the current estimate for Earth’s core¹³. Note that our choices for the time and magnetic field units differ slightly (by less than 5%) from ref.¹⁸, as we adopt the same units across all simulations. This change is made to obtain a consistent comparison between the original path models and those with a modified setup (Midpath-S, I and H, Supplementary Table 1) introduced in this study. Finally, the density anomaly rescaling used in Supplementary Video 4 follows from the velocity rescaling and from adjustment of the dimensionless, time-averaged convective power in the shell to an estimate¹⁷ $P = 3$ TW of the geodynamo power.

Stratified core case. The Midpath-S model (Supplementary Table 1) explores the effects of a possible upper outer core stratification⁴⁶ on the occurrence of simulated jerks. Within the Boussinesq approximation, stratification is modelled by adding an adverse density anomaly gradient³⁵ to the background gradient prescribed by the neutral buoyancy conditions described above:

$$\frac{dC}{dr} = \frac{-N^2\rho}{2g_o} (1 + \tanh((r-r_s)/\delta)) \tag{9}$$

Here N is the Brunt–Väisälä frequency pertaining to the stratification level at the core surface, $r_s = 3340$ km is the radius at which stratification sets in and $\delta = 10^{-2}D = 22.6$ km is the thickness of the stratified layer front. The thickness of the stratified layer is $r_o - r_s = 140$ km, as proposed in ref.⁴⁶. In the Midpath-S model we set $N = \Omega$, as also proposed in ref.⁴⁶. The output of the Midpath-S model demonstrates the preservation of simulated jerks against core stratification, albeit at a reduced energy level given the modifications of the background magnetic field that guides the waves.

Jerk energy definition, jerk identification and scaling. In Fig. 1c,d, we present the energy E_{SA} of the magnetic acceleration, defined as a mean-squared average over Earth’s surface S_E :

$$E_{SA} = \langle (\partial_t^2\mathbf{B})^2 \rangle = \frac{1}{S_E} \int_{S_E} \left(\frac{\partial^2\mathbf{B}}{\partial t^2} \right)^2 dS \tag{10}$$

Jerks are detected in the geomagnetic field models and the numerical simulations through a common procedure that evaluates changes in the magnetic acceleration. The instantaneous rate-of-change of acceleration is not reliably accessible in geomagnetic field models because of their limited temporal resolution, and we therefore define the jerk energy E_J as a sliding difference between consecutive time windows of finite width Δt :

$$E_J(t) = \langle (|\partial_t^2\mathbf{B}|_t^{t+\Delta t} - |\partial_t^2\mathbf{B}|_{t-\Delta t}^t)^2 \rangle \tag{11}$$

As introduced above, the angle brackets denote the average over Earth’s surface, and the square brackets denote a time average. Possible choices of Δt (Supplementary Fig. 5) are bounded by two constraints. The lower bound is the

temporal resolution^{6,7} (approximately 3 yr) of geomagnetic acceleration at spherical harmonic degree 9 in recent field models. Furthermore, for E_j to discriminate anomalously strong acceleration changes from those naturally created by the background convection, the upper bound of Δt is the typical timescale τ_{SA} for convectively driven-secular acceleration¹⁸. In all numerical models, along the parameter space path and in geomagnetic estimates, this timescale has a constant value^{18,47} $\tau_{SA} \approx 10$ yr at spherical harmonic degrees 1–9. These tight bounds imply that Δt should be kept relatively constant along the parameter space path, leading to our common choice $\Delta t = 3$ yr for the geomagnetic field model and the numerical simulations. Locating pulses in E_j suffices to identify jerks in the simulations because a change in the secular acceleration polarity is systematically obtained through the wave-driven jerk mechanism outlined in this study, and also matches the earlier determinations^{7–10} of jerk epochs when analysing the recent geomagnetic field. Moving along the parameter space path towards Earth's core conditions while keeping Δt constant also enables a quantitative extrapolation of simulated jerks energies for comparison with geomagnetic jerks. To this end, jerk recurrence statistics are obtained in Fig. 4b from time series (Fig. 4a) of E_j , by dividing the duration of the model run with the number of samples reaching or exceeding a given jerk energy. In Supplementary Fig. 2, jerk energies at 10, 30 and 100 yr recurrence times are extracted from Fig. 4b and scaled with ϵ , revealing a common dependency in $\epsilon^{-0.19 \pm 0.01}$. The end-of-path prediction in Fig. 4b is obtained by first extracting a single master curve from this scaling and the four energy-occurrence curves of Fig. 4b, and then extrapolating the master curve to the end-of-path conditions corresponding to $\epsilon = 10^{-7}$.

The typical energy E_{SA}^0 of geomagnetic acceleration away from pulse events is approximately constant along the parameter space path¹⁸. The E_j value can be obtained by estimating the amplification of E_{SA}^0 that follows from focusing of the azimuthal flow velocity or magnetic field perturbation carried by the wave. At Earth's surface, where E_j is evaluated, the increase in energy due to lateral focusing is mitigated by its migration to smaller and more attenuated lateral scales. Radial focusing is immune to this effect and occurs from the typical length d of a magnetic structure down to the skin depth $\delta_M = \sqrt{\eta r_A}$ of the magnetic boundary layer at the wave time scale, leading to

$$E_j \approx E_{SA}^0 \left(\frac{d}{\delta_M} \right)^2 \approx \left[E_{SA}^0 \left(\frac{d}{D} \right) \right]^2 \frac{\tau_\eta}{\tau_A} \quad (12)$$

The term between brackets represents the variability of jerk energy within a given model, and the factor¹⁷ $\tau_\eta/\tau_A \approx \epsilon^{-0.25}$ represents the systematic evolution of this energy along the parameter space path, in good agreement with the numerical result $E_j \approx \epsilon^{-0.19}$. The residual discrepancy stems from a slight variability of E_{SA}^0 along the path, following that¹⁷ of B .

Identification of quasi-geostrophic Alfvén waves. In Supplementary Fig. 1 we repeat the analysis carried out in ref. 18 to identify hydromagnetic wave propagation. The flow acceleration patterns that we analyse have a columnar structure that derives from the dominant rotational constraint of the Coriolis force. At any given t , cylindrical radius s and at a fixed analysis longitude φ_0 , we therefore first compute the columnar average $\partial u_\phi/\partial t$ of azimuthal flow acceleration:

$$\frac{\partial u_c}{\partial t}(s, \varphi_0, t) = \frac{1}{z_+ - z_-} \int_{z_-}^{z_+} \frac{\partial(\mathbf{u} \cdot \mathbf{e}_\varphi)}{\partial t}(s, \varphi_0, z, t) dz \quad (13)$$

Here s , φ and z are cylindrical coordinates, \mathbf{e}_φ is the unit vector in the azimuthal direction and the vertical integral is evaluated between the lower and upper heights z_{\pm} of an axial column parallel to the rotation vector $\boldsymbol{\Omega}$ at s . We then plot time-cylindrical radius maps of $\partial u_\phi/\partial t$ and overlay ray-tracing theoretical propagation tracks obtained by integrating in time the column-averaged Alfvén velocity c_A and column-averaged cylindrical radial fluid velocity V_r :

$$c_A(s, \varphi_0, t) = \sqrt{\frac{1}{z_+ - z_-} \int_{z_-}^{z_+} \frac{(\mathbf{B} \cdot \mathbf{e}_s)^2}{\rho \mu}(s, \varphi_0, z, t) dz} \quad (14)$$

$$V_r(s, \varphi_0, t) = \frac{1}{z_+ - z_-} \int_{z_-}^{z_+} \mathbf{u}(s, \varphi_0, z, t) \cdot \mathbf{e}_s dz \quad (15)$$

Here \mathbf{e}_s is the unit vector in the cylindrical radial direction. The adherence of $\partial u_\phi/\partial t$ to the Alfvén tracks and deviation from material upwelling tracks demonstrate Alfvén wave propagation.

Length-of-day variations. The numerical simulation solves for the deviations Ω_M of the mantle angular velocity from the background Ω (see ref. 45 for details):

$$I_M \frac{d\Omega_M}{dt} = \Gamma_M + \Gamma_G \quad (16)$$

Here I_M is the Earth's mantle moment of inertia, and $\Gamma_{M,G}$ are the magnetic and gravitational torques felt by the mantle, respectively. The corresponding rate of change in the length of the day (LOD) is then

$$\frac{d(\text{LOD})}{dt} = -\frac{2\pi}{\Omega^2} \frac{d\Omega_M}{dt} \quad (17)$$

where we have used $\Omega_M \ll \Omega$. Time series of $d(\text{LOD})/dt$ in the vicinity of jerk events are presented in Supplementary Fig. 4. The magnetic acceleration pulses cause pulses in $d^2\Gamma_M/dt^2$, and hence rapid inflexions in $d(\text{LOD})/dt$ with a shape similar to that observed in geodetic time series^{24,37}. Note that the amplitude of the inflexions is, as expected, significantly weaker in the numerical simulations than in Earth's core, because the inverse squared Alfvén number $(\tau_\eta/\tau_A)^2$ measuring the relative importance of magnetic forces and inertia is about 50 times weaker¹⁷ in the Midpath model than in the core.

Numerical implementation. Our numerical implementation involves a decomposition of the fields in spherical harmonics up to degree and order 133, and a discretization in the radial direction on a second-order finite-differencing scheme (see ref. 17 for numerical resolution details). We use the spherical harmonics transform library⁴⁸ SHTns, which is freely available at <https://bitbucket.org/nschaeff/shtns>. Time-stepping is semi-implicit, with second-order accuracy. Angular momentum conservation is controlled at each time step. To handle the increasing hydrodynamic turbulence along the path that only weakly affects the large-scale solution¹⁷, hyperdiffusion is implemented on the velocity and density anomaly fields, but not on the magnetic field, which remains natively resolved. The details, physical justification and validation of this approximation are presented in ref. 17. Each model on the path is initialized using the output of the previous step. Integration times after statistical equilibration are listed in Supplementary Table 1. In our main models, these represent at least 18% of a given magnetic diffusion time and 75% of a dipole decay time $r_0^2/\pi^2\eta$. Within this time, all model outputs are in a statistically steady state¹⁸ demonstrating self-sustained dynamo action. In particular, all models produced an axial dipole-dominated magnetic field that did not reverse polarity.

Data availability

The data that support the findings of this study are available from the corresponding author on request.

Code availability

The numerical simulation code used to generate the results of this study is available from the corresponding author on request.

References

- Pichon, G., Aubert, J. & Fournier, A. Coupled dynamics of Earth's geomagnetic westward drift and inner core super-rotation. *Earth Planet. Sci. Lett.* **437**, 114–126 (2016).
- Buffett, B. A. Geomagnetic fluctuations reveal stable stratification at the top of the Earth's core. *Nature* **507**, 484–487 (2014).
- Christensen, U. R., Wardinski, I. & Lesur, V. Timescales of geomagnetic secular acceleration in satellite field models and geodynamo models. *Geophys. J. Int.* **190**, 243–254 (2012).
- Schaeffer, N. Efficient spherical harmonic transforms aimed at pseudospectral numerical simulations. *Geophys. Geochem. Geosyst.* **14**, 751–758 (2013).

In the format provided by the authors and unedited.

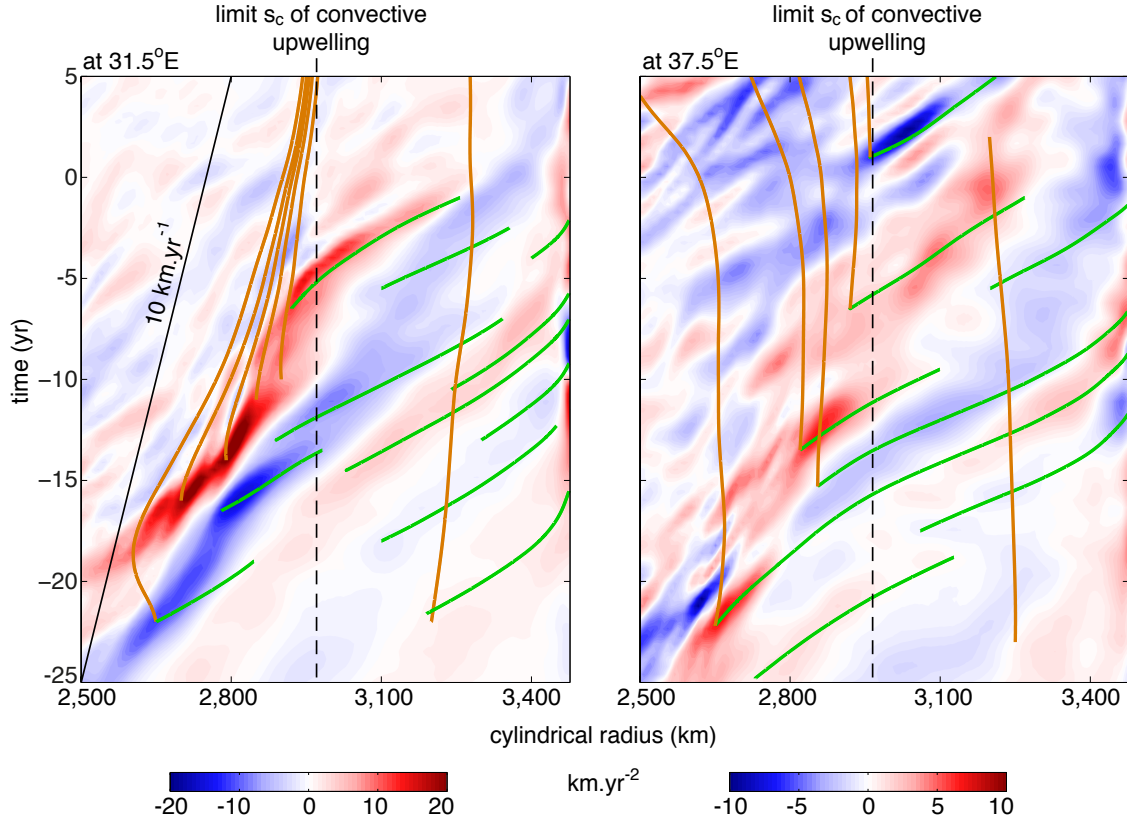
Geomagnetic jerks and rapid hydromagnetic waves focusing at Earth's core surface

Julien Aubert ^{1*} and Christopher C. Finlay ²

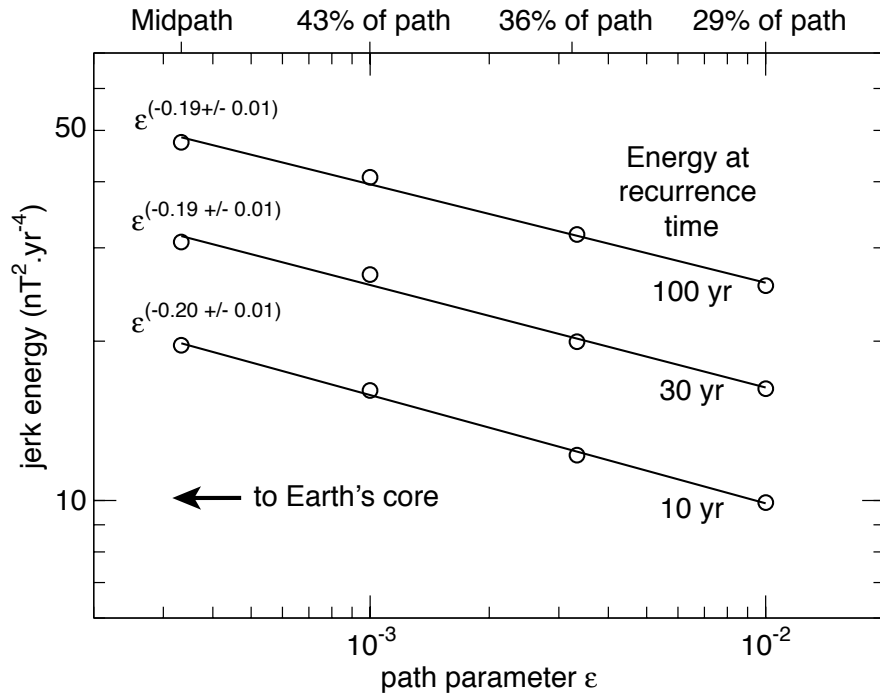
¹Université de Paris, Institut de Physique du Globe de Paris, CNRS, Paris, France. ²Division of Geomagnetism, National Space Institute, Technical University of Denmark, Lyngby, Denmark. *e-mail: aubert@ipgp.fr

Label	Path parameter ϵ	Path position	$\frac{\Delta\sigma_m}{D\sigma_c}$	core surface buoyancy	τ_U (yr)	τ_A (yr)	τ_Ω (yr)	Integration time (yr)
	10^{-2}	29%	10^{-4}	neutral	129	31.5	1.0	42 900
	$3.33 \cdot 10^{-3}$	36%	10^{-4}	neutral	126	24.0	0.6	34 600
	10^{-3}	43%	10^{-4}	neutral	123	18.2	0.3	24 900
Midpath	$3.33 \cdot 10^{-4}$	50%	10^{-4}	neutral	125	14.3	0.2	24 400
Midpath-I	$3.33 \cdot 10^{-4}$	50%	0	neutral	120	14.2	0.2	11 400
Midpath-H	$3.33 \cdot 10^{-4}$	50%	10^{-3}	neutral	128	14.6	0.2	11 300
Midpath-S	$3.33 \cdot 10^{-4}$	50%	10^{-4}	adverse	121	14.5	0.2	10 100
End of path	10^{-7}	100%			130	1.9	$3.2 \cdot 10^{-3}$	
Earth					≈ 140	≈ 2	$2.7 \cdot 10^{-3}$	

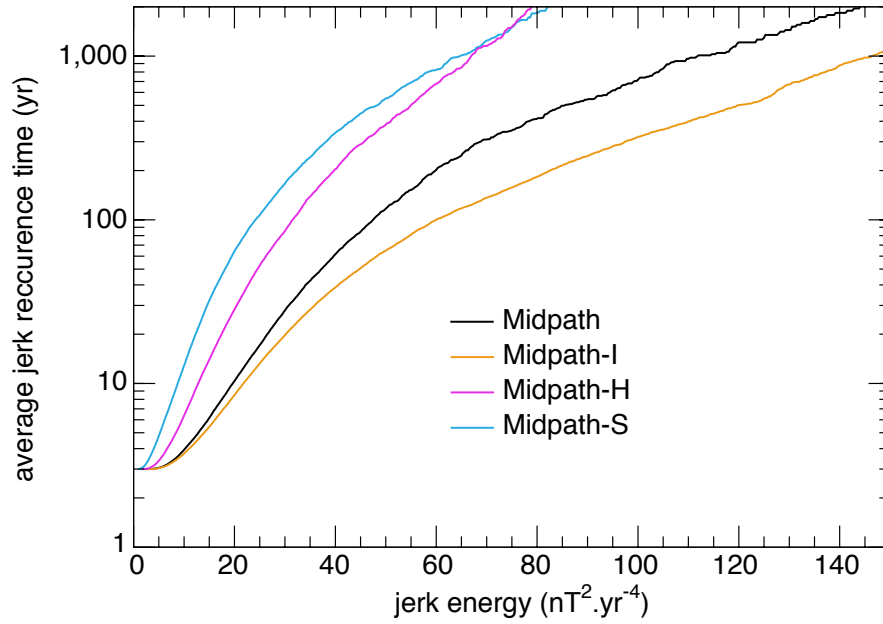
Supplementary Table 1: **Models along a parameter space path to Earth’s core.** Key parameters and corresponding dimensional time scale values for numerical models located along a parameter space path¹⁷ towards Earth’s core conditions. See Methods for definitions and ref. ¹⁸ for complete parameter data. Dimensional time scales values are obtained from the dimensionless time scale ratios reported in ref. ¹⁸ and the magnetic diffusion time scale set to $\tau_\eta = 135\,000$ yr in this study. Also shown are the values, closely approaching Earth’s core estimates, obtained by extrapolating scaling laws determined along the path¹⁷ to its end point.



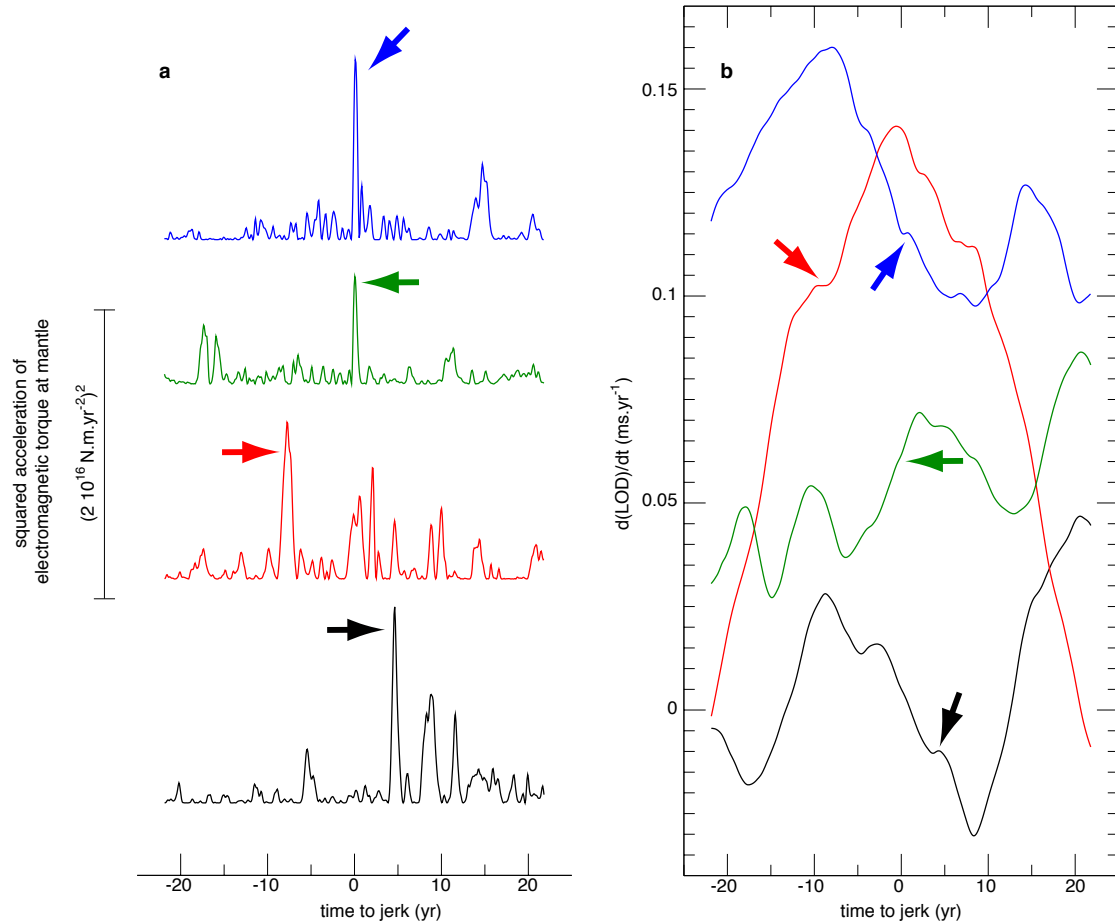
Supplementary Figure 1: **Alfvén wave propagation in the upper outer core.** Time-cylindrical radius diagrams of the column-averaged azimuthal flow acceleration $\partial u_c / \partial t$ (blue is westwards, see Methods for definitions) evaluated at two analysis longitudes, 31.5°E (as in Fig. 3b) and 37.5°E. Similar to ref. ¹⁸, green and brown curves respectively represent the ray-tracing theoretical propagation tracks of hydromagnetic waves at the column-averaged Alfvén speed c_A , and of material advection at the column-averaged cylindrical radial fluid velocity V_s . The slanted black line on the left panel denotes upward propagation at a speed 10 km/yr.



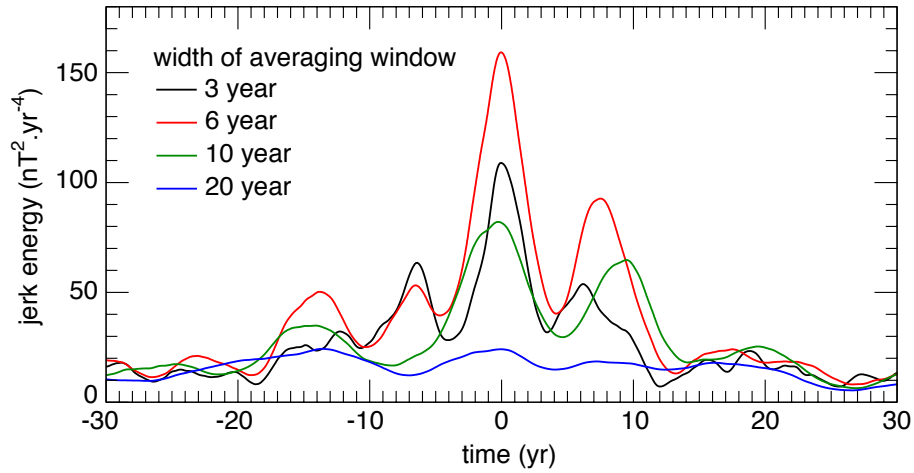
Supplementary Figure 2: **Scaling of jerk energy along the parameter space path.** Evolution of jerk energy at recurrence times 10, 30 and 100 years, as extracted from Fig. 4b, with the path parameter ϵ (Methods and Supplementary Table 1).



Supplementary Figure 3: **Sensitivity of the jerk recurrence time distribution to physical conditions in the lower mantle and upper outer core.** Distribution of the average recurrence time of jerks reaching or exceeding a given energy (same as Fig. 4b), for the models Midpath-I and Midpath-H with variable lower mantle electrical conductance, and model Midpath-S with a stratified region in the upper outer core (Methods). The Midpath model result from Fig. 4b is also reproduced for reference.



Supplementary Figure 4: **Signature of simulated jerks in the length of the day.** **a**, Squared acceleration $(d^2\Gamma_M/dt^2)^2$ (see Methods for definitions) of the electromagnetic torque exerted on the mantle by the outer core, as a function of time in the vicinity of four jerk events of model Midpath-H. **b**, first time derivative $d(\text{LOD})/dt$ of the simulated length of the day, as a function of time during the same jerk events. Arrows locate the pulses in the torque accelerations, that correspond to rapid inflexions in the rate of change of the length-of-day.



Supplementary Figure 5: **Choice of an averaging window width to define the jerk energy.** Time series of jerk energy E_J from the Midpath simulation, in the vicinity of the main jerk event at time 0 yr, obtained with various choices of the sliding averaging window width Δt (see Methods). The value $\Delta t = 3$ yr is adopted for all simulations and geomagnetic data in Figs. 1,4, Supplementary Figs. 2,3.

Supplementary Movie 1: Hammer projection of the core surface radial secular geomagnetic acceleration (orange is outwards) from the CHAOS-6x5 geomagnetic field model⁵, filtered at spherical harmonic degree 9, and spanning epochs 1999 to 2018.

Supplementary Movie 2: Hammer projection of the core surface radial secular geomagnetic acceleration (orange is outwards) from the Midpath model, filtered at spherical harmonic degree 9, in the vicinity of the jerk event occurring at time 0 yr.

Supplementary Movie 3: Hammer projection of the core surface azimuthal flow acceleration (blue is westwards) from the Midpath model, in the vicinity of the jerk event occurring at time 0 yr.

Supplementary Movie 4: Partial equatorial cut (left) and meridional cut outside the tangent cylinder (right) of the convective density anomaly (orange denotes lighter fluid) from the Midpath model in the vicinity of the jerk event occurring at time 0 yr. The meridional cut in the right panel is taken at the analysis longitude marked by a black line in the left panel.

Supplementary Movie 5: Partial equatorial cut (left) and meridional cut outside the tangent cylinder (right) of azimuthal flow acceleration (blue is westwards) from the Midpath model in the vicinity of the jerk event occurring at time 0 yr. The meridional cut in the right panel is taken at the analysis longitude marked by a black line in the left panel.

5. Finlay, C. C., Olsen, N., Kotsiaros, S., Gillet, N. & Tøffner-Clausen, L. Recent geomagnetic secular variation from Swarm and ground observatories as estimated in the CHAOS-6 geomagnetic field model. *Earth, Planets and Space* **68**, 112 (2016).
17. Aubert, J., Gastine, T. & Fournier, A. Spherical convective dynamos in the rapidly rotating asymptotic regime. *J. Fluid. Mech.* **813**, 558–593 (2017).
18. Aubert, J. Geomagnetic acceleration and rapid hydromagnetic wave dynamics in advanced numerical simulations of the geodynamo. *Geophys. J. Int.* **214**, 531–547 (2018).